James C. Iatridis

Assistant Professor,
Dept. of Mechanical Engineering,
University of Vermont,
Burlington, VT 05405-0084

Jeffrey P. Laible

Professor,
Dept. of Civil & Environmental Engineering,
University of Vermont,
Burlington, VT 05405-0084

Martin H. Krag

Professor,
Dept. of Orthopaedics and Rehabilitation,
and Vermont Back Research Center,
University of Vermont,
Burlington, VT 05405-0084

Influence of Fixed Charge Density Magnitude and Distribution on the Intervertebral Disc: Applications of a Poroelastic and Chemical Electric (PEACE) Model

A 3-dimensional formulation for a poroelastic and chemical electric (PEACE) model is presented and applied to an intervertebral disc slice in a 1-dimensional validation problem and a 2-dimensional plane stress problem. The model was used to investigate the influence of fixed charge density magnitude and distribution on this slice of disc material. Results indicated that the mechanical, chemical, and electrical behaviors were all strongly influenced by the amount as well as the distribution of fixed charges in the matrix. Without any other changes in material properties, alterations in the fixed charge density (proteoglycan content) from a healthy to a degenerated distribution will cause an increase in solid matrix stresses and can affect whether the tissue imbibes or exudes fluid under different loading conditions. Disc tissue with a degenerated fixed charge density distribution exhibited greater solid matrix stresses and decreased streaming potential, all of which have implications for disc nutrition, disc biomechanics, and tissue remodeling. It was also seen that application of an electrical potential across the disc can induce fluid transport. [DOI: 10.1115/1.1533804]

1 Introduction

Degenerative changes to the intervertebral disc are commonly implicated in low back pain and other disorders of the spine resulting in tremendous associated health care costs and disability [1,2]. One of the most significant changes to the intervertebral disc with degeneration and aging is the loss of proteoglycans, particularly in the nucleus pulposus [3–5]. Disc degeneration also resulted in a loss of swelling pressure [6–9], altered streaming potential [10] and an alteration of the hydraulic permeability [11]. The effect of a loss of fixed charge density on the fluid transport, pressurization, streaming potential and streaming current in the disc has not been examined in a two dimensional configuration.

The intervertebral disc may be described as a charged, hydrated and permeable material. It is comprised largely of collagen and elastic fibers embedded in a proteoglycan gel to form a solid matrix. The proteoglycans contain many glycosaminoglycan chains with fixed sulfate (SO_4) and carboxyl (COOH) groups. Under physiological concentrations and pH (assumed to be NaCl $=0.15$ M, pH$=7.4$) these groups are negatively charged. Mobile positive and negative ions in the extrafibrillar water form an electrolyte solution. The high fixed charge density is responsible for generating osmotic pressure, streaming potential and other electrochemical phenomena and also contributes to the hydration and compressive strength of the tissue [12–17]. The fixed charge density distribution along the sagittal plane of a 26 year old and 74 year old disc were given by Urban & Holm [5].

Multiphasic continuum and computational models have been applied to the analysis of the mechanical, electrical, and chemical behaviors of the intervertebral disc [6,10,11,18–24]. In these studies, viscoelastic behaviors are generally assumed to be related to

frictional drag between the solid and fluid phases, although intrinsic solid matrix viscoelasticity has also been described [25]. The disc also behaves like a semipermeable membrane allowing the passage of water and ions but prohibiting the motion of the fixed negative charges. The effects of swelling and transport were introduced in continuum descriptions of soft-tissue mechanics in a variety of ways. Poroelastic finite element models were developed for the intervertebral disc [18,23]. In these models the "relative" fluid velocities are used. The relative view is routinely used in poroelastic theory [26,27] and in "$u-w$" poroelastic models, most recently presented in Simon et al. [28,29] and Laible et al. [22] where swelling effects were included. Importantly, the triphasic theory [15] provides a link between mechanical theories and electro-chemical theories. The triphasic theory including electrical effects was used in a one dimensional model to examine streaming potential in soft tissue [14,30]. In addition to these studies, triphasic phenomena (termed quadriphasic in these studies to distinguish between anions and cations) were investigated using a commercial FE package in a geometrically nonlinear model [20,24,31].

The PEACE model uses the field variables of solid displacement u, relative fluid velocity w, electric potential Φ, and Cl concentrations c^- and Na concentrations c^+ (obtained from electro neutrality). The formulation uses poroelastic theory directly using a $u-w$ formulation which distinguishes it from the multiphasic models of [14,20,24,30,31] in which pressure is used as a field variable. One goal of the model was to explicitly identify the relation of the phenomenological equations to the basic frictional coefficients. A mobility relation details this relation in a form that relates: the fluid flux, the current, the positive ion flux and the negative ion flux to the fluid potential, the electric potential, the positive ion chemical potential and the negative ion chemical potential.

In the present study, we present a 3-dimensional formulation for a hydrated and charged porous media which draws heavily from the work of Gu et al. [14] and Simon et al. [29]. The objectives of this study were to: 1) derive a set of equations for a 3-dimensional

poroelastic and chemical electric (PEACE) material that can readily be solved by standard finite element techniques; 2) validate the model using 1-dimensional experimental results, 3) demonstrate the utility of the PEACE model via a 2-dimensional diagnostic version applied to a slice of intervertebral disc; 4) investigate the influence of fixed charge density magnitude and distribution on water transport on the disc slice; and 5) investigate the effect of applied electric potential on water transport in the same disc slice.

2 Development of the PEACE Equations

2.1 Combined Equations for the PEACE Model. In the development of the **PEACE** model we consider the tissue to be composed of a solid matrix phase, a fluid phase and the positive and negative ion phases. We first write the equations in a primitive form and then proceed to derive a set of equations that can be readily solved by standard finite element procedures. The numerical formulation uses the Galerkin finite element method (GFEM) for spatial discretization and an implicit finite differences scheme for temporal discretization. In the process of forming the equations that can be solved by the GFEM, we trace the physical coefficients to the more familiar phenomenological coefficients. This process was done symbolically using Maple (Scientific Workplace V3.0, MacKichan Software, Inc., Bainbridge Island, WA).

The momentum equations represent the balance of the forces acting on each phase. These equations are written in terms of the forces per unit volume of the tissue. The forces arise from pressure gradients, internal frictional forces between the phases, external body forces due to gravitational and electrical fields and in the case of accelerated motion the inertial forces. Here we will only consider very slow motion and hence the latter may be neglected. The momentum equations for the four phases in terms of a control volume of the tissue (which we also refer to as the mixture) are a variant of those equations found from Gu et al. [14]:

$$-\rho_s(\nabla \cdot \boldsymbol{\mu}_s)^T + f_{s,w}(v_w - v_s) + f_{p,s}(v_p - v_s) + f_{n,s}(v_n - v_s)$$
$$- nc^F F E = 0 \tag{1}$$

$$-\rho_w \nabla \mu_w + f_{s,w}(v_s - v_w) + f_{w,p}(v_p - v_w) + f_{w,n}(v_n - v_w) = 0 \tag{2}$$

$$-\rho_p \nabla \mu_p + f_{p,s}(v_s - v_p) + f_{w,p}(v_w - v_p) + f_{p,n}(v_n - v_p)$$
$$+ nc^p F E = 0 \tag{3}$$

$$-\rho_n \nabla \mu_n + f_{n,s}(v_s - v_n) + f_{w,n}(v_w - v_n)$$
$$+ f_{p,n}(v_p - v_n) - nc^n F E = 0 \tag{4}$$

where: s, w, p, n refer to the solid, water, positive ion and negative ion phases, ρ_i are densities (kg/m^3), c_i are concentrations, v_i are absolute velocities, $f_{i,j}$ are drag coefficients, μ_w, μ_p and μ_n are scalar potentials, $\boldsymbol{\mu}_s$ is σ_s / ρ_s (where σ_s is the solid stress), n is porosity, c^F is the fixed charge density, $E = -\nabla \Phi$ is the electrical field strength, Φ is the electric potential, and F is Faraday's constant. A superscript implies a measurement per volume of water and a subscript implies a measurement per volume of the mixture. The parameter μ_s is the solid potential which can be related to the solid matrix stress.

The velocity of the fluid and ions relative to the solid matrix can be expressed as

$$\frac{\dot{w}_w}{n} = (v_w - v_s) \tag{5}$$

$$\frac{\dot{w}_p}{n} = (v_p - v_s) \tag{6}$$

$$\frac{\dot{w}_n}{n} = (v_n - v_s) \tag{7}$$

The potential for the positive and negative ions can be expressed as:

$$\rho_p \nabla \mu_p = nc^p M_p \frac{RT}{c^p M_p} \nabla c^p = nRT \nabla c^p \tag{8}$$

$$\rho_n \nabla \mu_n = nc^n M_n \frac{RT}{c^n M_n} \nabla c^n = nRT \nabla c^n \tag{9}$$

The current is the difference in the motion of the positive and negative ions and can be expressed as:

$$I_e = F[c^p - c^n] \begin{Bmatrix} \dot{w}_p \\ \dot{w}_n \end{Bmatrix} \tag{10}$$

Using the relative velocity equations 5–7, the chemical potential equations 8–9 and the current equation 10, the momentum equations for the fluid and ions (2–4) can be manipulated to yield a **mobility relation** that relates 1) the fluid velocity $\dot{w}_w$, 2) the current I_e, 3) the positive ion velocities $\dot{w}_p$ and 4) the negative ion velocities $\dot{w}_n$ to: 1) the fluid potential gradient $\nabla \mu_w$, 2) the electric potential gradient $\nabla \Phi$, 3) the gradient of the positive ion concentration ∇c^p and 4) the gradient of the negative ion concentration ∇c^n. In a matrix form the relation is:

$$
\begin{Bmatrix} \dot{w}_w \\ I_e \\ \dot{w}_p \\ \dot{w}_n \end{Bmatrix}
=
\overbrace{
\begin{bmatrix}
-\dfrac{1}{k_w} & F\nu_w & -\dfrac{k_p}{k_w} & -\dfrac{k_n}{k_w} \\
F\nu_w & F^2(\nu_p c^p - \nu_n c^n) & F\nu_p & F\nu_n \\
-\dfrac{k_p}{k_w} & F\nu_p & -\dfrac{\alpha_p}{D/n} & -\dfrac{f_{w,n}f_{w,p}}{D/n} \\
-\dfrac{k_n}{k_w} & F\nu_n & -\dfrac{f_{w,n}f_{w,p}}{D/n} & -\dfrac{\alpha_n}{D/n}
\end{bmatrix}
}^{\text{MOBILITY MATRIX}}
\begin{Bmatrix} \rho_w \nabla \mu_w \\ n\nabla \Phi \\ nRT\nabla c^p \\ nRT\nabla c^n \end{Bmatrix}
\tag{11}
$$

The terms in the MOBILITY MATRIX of equation 11 were obtained symbolically in terms of the original friction terms in equation 1–4 using Maple and are defined in Appendix A. The first row of equation 11 is a generalization of Darcy's law in the presence of electrical and chemical potential gradients. Note that the MOBILITY MATRIX is symmetric. It is interesting to note that the term k_w is the inverse permeability and is given in terms of the friction coefficients $f_{i,j}$ and the porosity n as:

$$k_w = \frac{1}{n}\left(f_{s,w} + \frac{f_{p,s}f_{w,p}}{f_{p,s}+f_{w,p}} + \frac{f_{n,s}f_{w,n}}{f_{n,s}+f_{w,n}} \right)$$

Further consideration of the mass conservation of the ions, the chemical potential of the fluid phase and the poroelastic equations for the fluid and solid phases, we can symbolically derive the final **PEACE** equations for the four phases.

SOLID PHASE

$$[L^T D_{\varepsilon,\varepsilon} \quad L^T D_{\varepsilon,\zeta}]\begin{bmatrix} L\mathbf{u} \\ \nabla \cdot \mathbf{w} \end{bmatrix} + L^T \boldsymbol{\sigma}_{o\sigma} = 0 \tag{12}$$

FLUID PHASE

$$-K_{w,w}\dot{\mathbf{w}} + \nabla[D_{\zeta,\varepsilon} \quad D_{\zeta,\zeta}]\begin{pmatrix} L\mathbf{u} \\ \nabla \cdot \mathbf{w} \end{pmatrix} - K_{w,\phi}\nabla\Phi - (K_{w,n}+K_{w,p})\nabla c^n - K_{w,p}\nabla c^F + \nabla \sigma_{o\pi} = 0 \tag{13}$$

ELECTRICAL PHASE

$$-\nabla \cdot K_{\phi,w}\dot{\mathbf{w}} + -\nabla \cdot K_{\phi,\phi}\nabla(\Phi) - \nabla \cdot (K_{\phi,n}+K_{\phi,p})\nabla c^n - \nabla \cdot K_{\phi,p}\nabla c^F = 0 \tag{14}$$

CHEMICAL PHASE

$$0*\dot{\mathbf{u}} + n\dot{c}^n + \nabla \cdot K_{n,w}\dot{\mathbf{w}} - \nabla \cdot (K_{n,n}+K_{n,p})\nabla c^n - \nabla \cdot K_{n,\phi}\nabla\Phi - \nabla \cdot K_{n,p}\nabla c^F = 0 \tag{15}$$

In these equations the four field variables are $\mathbf{u}$, $\mathbf{w}$, Φ, c^n (solid displacement, fluid displacement, electrical potential and negative ion fields, respectively). The terms in these equations are defined in Appendix B. The equations [12–15] are the counterparts of equations 37, 41, and 42, found in Sun et al. [30]. The finite element form for the general 3D problem, via the Galerkin FEM method are given in Appendix C. In the following we will consider a 2D form of the equations, representing a horizontal slice of an intervertebral disc at the mid plane.

2.2 1D Validation Study. The PEACE model was used to simulate the load displacement response as obtained by Drost, et al. [32]. That study considered the compression of the canine annulus under chemical and mechanical loading. Anulus fibrosus specimens were tested in a confined compression creep experiment where the displacement of the top of a $d=4$ mm diameter, $h=1$ mm thick disc plug was measured. The circumference of the plug was confined by the impermeable wall of the holder, the bottom rested on a porous filter and the top was loaded by an impermeable piston. The plug was subjected to a sequence of load stages in which the NaCl bath concentration c^* and load P were varied (Fig. 1). Using the PEACE model the we simulated the following load stages 1) Conditioning, $c^*=0.6$ M, $P=0.08$ MPa, 2) Swelling, $c^*=0.2$ M, $P=0.08$ MPa and 3) Consolidation, $c^*=0.2$ M, $P=0.20$ MPa. Curves a, b and c (Fig. 1) show the PEACE model response at the top, middle, and bottom

quarter height of the specimen, $h=1$ mm, 0.5 mm and 0.25 mm respectively. For the 1 dimensional PEACE simulation, material parameters were taken from Drost et al., [32].

2.3 2D Diagnostic Analysis: Finite Element Formulation. We consider a two dimensional version the equations, to analyze a horizontal slice of the disc. We reduce the three dimensional equations to a horizontal plane stress problem, in which we incorporate a vertical compressive total stress ($\sigma_{z,z}$) as an initial stress. This requires modification of the **three dimensional** isotropic solid-fluid constitutive equation:

$$\begin{Bmatrix} \sigma \\ \pi \end{Bmatrix} = \left[\begin{bmatrix} \mathbf{D}_s & 0 \\ 0 & 0 \end{bmatrix} + \begin{bmatrix} mQm^T & mQ \\ m^T Q & Q \end{bmatrix} \right] \begin{Bmatrix} \mathbf{e} \\ \zeta \end{Bmatrix} + \begin{Bmatrix} \boldsymbol{\sigma}_{o\sigma} \\ \sigma_{o\pi} \end{Bmatrix} \tag{16}$$

$$\mathbf{D}_s = \begin{bmatrix} D_{\varepsilon,\varepsilon} & D_{\varepsilon,\mu} \\ D_{\mu,\varepsilon} & D_{\mu,\mu} \end{bmatrix} D_{\varepsilon,\mu} = D_{\mu,\varepsilon}^T = 0,$$

$$D_{\mu,\mu} = \delta_{i,j}\mu \quad \text{with } i \quad \text{and} \quad j=1,2,3$$

$$D_{\varepsilon,\varepsilon} = \delta_{i,j}(\lambda+2\mu) + (1-\delta_{i,j})\lambda,$$

$$\lambda = \frac{\nu E}{(1+\nu)(1-2\nu)}, \quad \mu = \frac{E}{2(1+\nu)}$$

$$\boldsymbol{\sigma} = [\sigma_{xx} \quad \sigma_{yy} \quad \sigma_{zz} \quad \sigma_{xy} \quad \sigma_{yz} \quad \sigma_{zx}]^T$$

$$\mathbf{e} = [\varepsilon_{xx} \quad \varepsilon_{yy} \quad \varepsilon_{zz} \quad \varepsilon_{xy} \quad \varepsilon_{yz} \quad \varepsilon_{zx}]^T$$
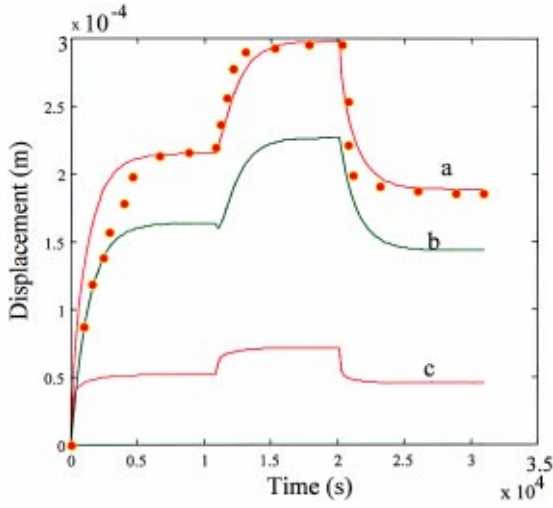
Fig. 1 Experimental results (circles, from Drost et al. 1995) and simulation of the PEACE model (curves a,b,c) for a 1 dimensional confined compression study of canine annulus under chemical and mechanical loading. Displacement of anulus fibrosus specimens (d=4 mm diameter, h=1 mm thick) was measured while the NaCl bath concentration c* and load P were varied in 3 stages: 1) Conditioning, c*=0.6 M, P =0.08 MPa, 2) Swelling, c*=0.2 M, P=0.08 MPa and 3) Consolidation, c*=0.2 M, P=0.20 MPa. Curves a, b and c show the PEACE simulation at h=1 mm, 0.5 mm and 0.25 mm, respectively.

For the **two dimensional** plane stress problem it is assumed that the vertical shear strains and stresses are zero. One can then solve for the vertical strain $\varepsilon_{z,z}$ in terms of the applied total stress $\sigma_{z,z}$, the strains $\varepsilon_{x,x}$, $\varepsilon_{y,y}$ and the fluid strain ζ, i.e.

$$\varepsilon_{z,z}=\frac{\sigma_{z,z}-(\lambda+Q)\varepsilon_{x,x}-(\lambda+Q)\varepsilon_{y,y}-Q\zeta}{(\lambda+2\mu+Q)}$$

With this relation, the constitutive equation for the **two dimensional** plane stress problem with an applied total stress normal to the plane, can be written as:

$$\begin{Bmatrix}\sigma\\\pi\end{Bmatrix}=\begin{bmatrix}D_{s,s} & D_{s,\zeta}\\D_{\zeta,s} & D_{\zeta,\zeta}\end{bmatrix}\begin{Bmatrix}\varepsilon\\\zeta\end{Bmatrix}+\begin{Bmatrix}\sigma_{o\sigma}\\\sigma_{o\pi}\end{Bmatrix} \quad (17)$$

$$\pi^c=-\rho_{w\mathbf{T}}\mu_{w,0}+RT\phi(2c^n+c^F)-B_w m^T\varepsilon+T_c \quad (18)$$

where:

$$D_{s,s}=\begin{bmatrix}\dfrac{4\mu(\lambda+\mu+Q)}{\lambda+2\mu+Q} & \dfrac{2\mu(\lambda+Q)}{\lambda+2\mu+Q} & 0\\[2ex]\dfrac{2\mu(\lambda+Q)}{\lambda+2\mu+Q} & \dfrac{4\mu(\lambda+\mu+Q)}{\lambda+2\mu+Q} & 0\\[2ex]0 & 0 & \mu\end{bmatrix},$$

$$D_{s,\zeta}=D_{\zeta,s}^T=\begin{pmatrix}\dfrac{2\mu Q}{\lambda+2\mu+Q}\\[2ex]\dfrac{2\mu Q}{\lambda+2\mu+Q}\\[2ex]0\end{pmatrix}, \quad \sigma_{\varepsilon,o}=\begin{pmatrix}\dfrac{(\lambda+Q)\sigma_{z,z}}{\lambda+2\mu+Q}\\[2ex]\dfrac{(\lambda+Q)\sigma_{z,z}}{\lambda+2\mu+q}\\[2ex]0\end{pmatrix}$$

$$D_{\zeta,\zeta}=\left(\frac{Q(\lambda+2\mu)}{\lambda+2\mu+Q}\right), \quad D_{\zeta,\zeta}=\left(\frac{Q(\lambda+2\mu)}{\lambda+2\mu+q}\right), \quad \sigma_{o\sigma}=\sigma_{\varepsilon,o},$$

$$\sigma_{o\pi}=\sigma_{\zeta,o}+\pi^c$$

$$\varepsilon^T=[\varepsilon_{x,x}\ \varepsilon_{y,y}\ \varepsilon_{x,y}],\ \ \sigma^T=[\sigma_{x,x}\ \sigma_{y,y}\ \sigma_{x,y}],$$

$$\sigma_{\zeta,o}=\left(\frac{Q}{\lambda+2\mu+q}\right)$$

$$\sigma_{z,z}$$

$$\varepsilon=L\mathbf{u},\ \ \zeta=\nabla\cdot\mathbf{w},\ \ L^T=\begin{bmatrix}\dfrac{\partial}{\partial x} & 0 & \dfrac{\partial}{\partial y}\\[2ex]0 & \dfrac{\partial}{\partial y} & \dfrac{\partial}{\partial x}\end{bmatrix},$$

$$\nabla\cdot=m^T L,\ \ m^T=[1\ \ 1\ \ 0]\ \ \mathbf{u}=\begin{Bmatrix}u_x\\u_y\end{Bmatrix},\ \ \mathbf{w}=\begin{Bmatrix}w_x\\w_y\end{Bmatrix}$$

In this study we also split the four equations into two sets, the chemical-electrical equations and the solid-fluid equations. Using the Galerkin finite element method, the chemical-electrical balance equations become:

$$\begin{bmatrix}0 & 0\\0 & \mathbf{M}_{cc}\end{bmatrix}\begin{Bmatrix}\dot{\boldsymbol{\Phi}}\\\dot{\mathbf{c}}\end{Bmatrix}+\begin{bmatrix}\mathbf{K}_{\phi\phi} & \mathbf{K}_{\phi c}\\\mathbf{K}_{c\phi} & \mathbf{K}_{cc}\end{bmatrix}\begin{Bmatrix}\boldsymbol{\Phi}\\\mathbf{c}\end{Bmatrix}=\begin{Bmatrix}\mathbf{P}_\phi\\\mathbf{P}_c\end{Bmatrix} \quad (19)$$

$$\mathbf{M}_{cc}=\langle N^T n N\rangle_\Omega,\ \ \mathbf{K}_{i,j}=\langle(\nabla N)^T K_{i,j}\nabla N\rangle_\Omega,\ \ i=\phi,c,\ \ j=\phi,c$$

$$\mathbf{P}_i=\langle N^T I_{in}\rangle_\Gamma-\langle(\nabla N)^T K_{i,p}\nabla N\rangle_\Omega \bar{c}^F+(-1)^k\langle(\nabla N)^T K_{i,w}\dot{\mathbf{w}}\rangle_\Omega$$

$$k=1,2\ \ \text{for}\ \ i=\phi,c,\ \text{respectively}$$

$\langle\cdot\rangle_{\Omega,\Gamma}$ implies integration over the domain and boundary respectively. $N=[N_1\ N_2\ N_3]$ are the linear triangular basis functions. The terms $I_{\phi n}$ and I_{cn} are the normal current and negative ion flux on the boundary. The system is nonlinear since the $K's$ depend on $c's$. The system has been solved by direct iteration using an assumed fixed set of nodal values of the fixed charged density, c^F. An initial c^n is computed from Donnan equilibrium at the boundary and defines the initial set of nodal values of $\bar{c}^n$. Using electroneutrality $\bar{c}^p=\bar{c}^n+\bar{c}^F$ the $K's$ are computed and the equations are solved for the nodal values of $\bar{\Phi}$ and $\bar{c}^n$. The process is repeated with the latest $\bar{c}^n$ and $\bar{c}^p=\bar{c}^n+\bar{c}^F$, until the nodal values converge. Only $2\rightarrow5$ iterations are necessary. We first solve the chemical-electrical equations for a steady condition with

$$\dot{c}^n=0,\quad \dot{\mathbf{w}}=0.$$

With $\dot{\mathbf{w}}$ and $\bar{c}^n$ defined, the solid-fluid equations will yield a value for a reanalysis.

Again using the Galerkin finite element method, the solid-fluid equations become:

$$\begin{bmatrix}\mathbf{0} & \mathbf{0}\\\mathbf{0} & \mathbf{M}_{ww}\end{bmatrix}\begin{Bmatrix}\dot{\mathbf{u}}\\\dot{\mathbf{w}}\end{Bmatrix}+\begin{bmatrix}\mathbf{K}_{uu} & \mathbf{K}_{uw}\\\mathbf{K}_{wu} & \mathbf{K}_{ww}\end{bmatrix}\begin{Bmatrix}\mathbf{u}\\\mathbf{w}\end{Bmatrix}=\begin{Bmatrix}\mathbf{P}_u\\\mathbf{P}_w\end{Bmatrix} \quad (20)$$

$$\mathbf{M}_{ww}=\langle\mathcal{N}^T\tilde{k}_w\mathcal{N}\rangle_\Omega,\ \ \mathbf{K}_{i,j}=\langle B_i^T D_{i,j}B_j\rangle_\Omega,\ \ i=\varepsilon,\zeta,\ \ j=\varepsilon,\zeta,$$

$$D_{2,2}=D_{\zeta,\zeta}+B_w$$

$$\mathbf{P}_u=-\langle B_\varepsilon^T D_{\varepsilon,o}N\bar{\sigma}_{z,z}\rangle_\Omega+\langle\mathcal{N}^T T_\sigma\rangle_\Gamma,\ \ B_\varepsilon=L\mathcal{N},\ \ B_\zeta=\nabla\cdot\mathcal{N},$$

$$B_s=\nabla N$$

$$\mathbf{P}_w = -\langle B_\zeta^T D_{\zeta,o} N \bar{\sigma}_{z,z} \rangle_\Omega + \langle \mathcal{N}^T T_\pi \rangle_\Gamma - \mathbf{P}_{\phi c},$$

$$\mathcal{N} = [N_1 \mathbf{I}_{22} \quad N_2 \mathbf{I}_{2,2} \quad N_3 \mathbf{I}_{2,2}]$$

$$\mathbf{P}_{\phi c} = \langle B_\zeta^T N \bar{\pi}^o \rangle_\Omega + \langle \mathcal{N}^T K_{w,\phi} B_s \bar{\Phi} + \mathcal{N}^T \tilde{K}_{w,n} B_s \bar{c}^n$$

$$+ \mathcal{N}^T K_{w,F} B_s \bar{c}^F \rangle_\Omega$$

$$\mathbf{I}_{2,2} = \begin{bmatrix} 1 & 0 \\ 0 & 1 \end{bmatrix}, \quad \mathfrak{N} = \begin{pmatrix} n_x & 0 \\ 0 & n_y \\ n_y & n_x \end{pmatrix}, \quad \mathfrak{n} = \begin{pmatrix} n_x \\ n_y \end{pmatrix}$$

$T_\sigma = \mathfrak{N}^T \boldsymbol{\sigma}$ and $T_\pi = \mathfrak{n}\pi$ are the total applied stress and total fluid pressure traction force components in the horizontal plane, with $\mathfrak{N}$, $\mathfrak{n}$=outward normal direction cosines operators. $\bar{\pi}^o$ are nodal values of the osmotic/chemical $(-\rho_{w\mathbf{T}}\mu_{w,0} + RT\phi(2c^n + c^F) + T_c)$ pressure and $\bar{\sigma}_{z,z}$ are nodal values of the applied stress normal to the plane.

2.4 Geometry, Material Properties, Boundary and Initial Conditions. A thin horizontal slice of the disc, 0.005m thick was used for the model (Fig. 2). The idealized horizontal plane dimensions and geometry were characteristic of a lumbar spine intervertebral disc. In the model, we assume that the top and bottom surfaces of the slice meet impermeable, insulated, frictionless, and rigid surfaces so that there is no vertical flow. On the periphery of the disc, fluid is free to flow but the fluid is subjected to an osmotic pressure as contained in the term π^c of equation 18. These conditions represent a slice at the mid elevation of a disc. In all analyses, the rigid body motion of the solid phase was prevented by providing a determinate support condition, solid displacements u_x and u_y were set to zero at a centered node and the u_y displacement was set to zero at a boundary node to prevent rigid body rotation. The concentration and electrical potential were prescribed at the boundaries. The c^n concentration at the boundary was established by equating internal and external chemical potentials at the boundary, i.e. the Donnan equilibrium condition $(c^n)^2 + c^n c^F - (c^*)^2 = 0$ (with $c^* = 0.2M$ around the periphery of the disc slice). The electric potential Φ at the boundary
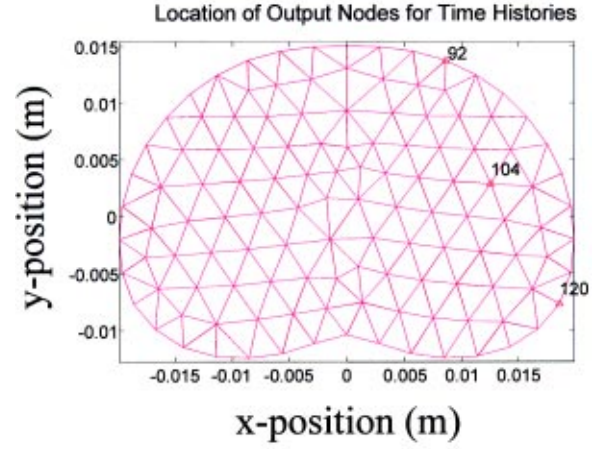

Location of Output Nodes for Time Histories

Fig. 2 Mesh for plane stress analysis of intervertebral disc slice. The numbers of three nodes are given for reference to the time histories of the loading and fluid flow.

was similarly obtained, which yields $\Phi = \Phi^* + RT/F \ln(c^n/c^*)$ or equivalently $\Phi = \Phi^* - RT/2F \ln(c^n + c^F/c^n)$, ($\Phi^* = 0$ around the periphery of the disc slice). The second term on the right hand side of either expression is called the *thermal potential* and is due to the difference in the ion concentrations of the surrounding body fluid and the concentration at the tissue surface.

These boundary values were used as the initial fields throughout the disc, to start the iterative solution process for the internal c^n and Φ fields. Once these fields were established, the $u-w$ solution was obtained by first allowing the disc to free swell in a saline bath of 0.2M NaCl concentration for 33 hours, at which point a constant compressive z stress of 200000 N/m^2 was applied for an additional 33 hours.

The following material property values were used for the analyses.

$$T = 310K \qquad R = 8318.78 \frac{liter - Pa}{mole - K}$$

$$F = 96500 \frac{coulomb}{mole}$$

$$f_{s,w} = 1.0*10^{15} \frac{N-s}{m^4} \qquad f_{w,p} = 5.0039*10^{14} \frac{N-s}{m^4}$$

$$f_{p,s} = 1.0*10^{10} \frac{N-s}{m^4} \qquad f_{n,s} = 1.0*10^{10} \frac{N-s}{m^4} \qquad f_{w,n} = \frac{79}{52} f_{w,p}$$

$$n = 0.70 = porosity$$

$$Q = 2*10^8 \frac{N}{m^2} \qquad E_{anulus} = 2.25*10^6 \frac{N}{m^2} \qquad B_w = 0.5*10^6 \frac{N}{m^2}$$

$$c^* = 0.2M \left(\frac{moles}{liter} \right) \qquad E_{nucleus} = \frac{1}{10} E_{anulus} \qquad \nu = 0.48$$

$$\gamma_n, \gamma_p, \gamma_n^*, \gamma_p^* = 1$$

For these values it was found that the T_c contribution was relatively small and hence T_c is set to zero. The constant bath concentration was denoted by c^*. The initial concentration just inside the disc was established by Donnan equilibrium. In an analysis with no applied potential we can set Φ^* to any constant value on the boundary since we are using a constant c^n and c^* on the boundary. The constant potential boundary condition will not provide any driving mechanism.

2.5 Fixed Charge Density Distribution. Three separate fixed charge density distributions were investigated: healthy, degenerate, and constant equivalent healthy. The fixed charge density distribution along the sagittal plane of a 26 year old and 74 year old disc (Fig. 3a, data taken from Urban & Holm, [5]) were used to generate a 2-dimensional c^F field over our finite element mesh for healthy (Fig. 3b) and degenerate (Fig. 3c) discs, respectively. For the 26 year old disc, there was a value of 0.15M at the
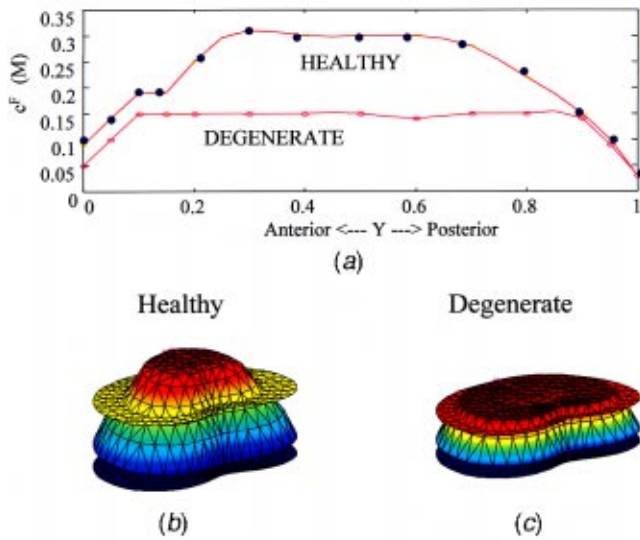
Fig. 3 Fixed charge density distribution for healthy and degenerate intervertebral discs in the sagittal plane. The experimental data was digitized from Urban & Holm, 1986. The healthy and degenerate fixed charge distribution (*a*) were used to generate a 2-dimensional c^F field over our finite element mesh for healthy (*b*) and degenerate (*c*) discs. The constant equivalent healthy fixed charge distribution c^F_{equiv} was taken as the average fixed charge density over the surface of the healthy disc and can be seen as the horizontal plane in (*b*).

edge of the disc and a peak value of 0.3 M at the center of the disc. The equivalent healthy fixed charge density was a constant distribution about the disc slice with a value defined by $c^F_{equiv} = 1/A \int c^F dA$, where c^F is the 26 year old sagittal fixed charge density distribution from Fig. 2*a* and A is the cross sectional area of the disc slice (Fig. 3*b*, horizontal plane).

2.6 Applied Electrical Potential. A numerical simulation was conducted to illustrate that fluid can be induced to flow through the disc by an altered electrical potential on the boundary of the disc. The natural thermal potential has a magnitude of $\Phi = RT/F \ln(c^n/c^*)\cdot$, where c^n is the Donnan equilibrium concentration at the boundary and c^* is the physiological fluid concentration in the fluid surrounding the boundary. For a variable fixed charge density, c^n and Φ will have a natural variation. At point *A* (in the postero-lateral anulus fibrosus) the potential was reduced by the natural potential Φ to make it zero. At point *B* (in the anterior anulus fibrosus) the potential was increase by the natural potential Φ to make it twice as large. For the healthy disc the two potentials at *A* and *B* are 0 and -10.75 mV, respectively. For the degenerate disc the two potentials at *A* and *B* are 0 and -6.3 mV, respectively.

3 Results

The 1-dimensional simulation (Fig. 1) demonstrated very good agreement between the experimental results for the displacement of the specimen (taken from the literature, [32]) and the PEACE model. The displacement is also given for nodes at the mid-height and bottom quarter where experimental data was not measured. This agreement validates our model in 1 dimension and demonstrates the ability of the model to simulate realistic physical data.

The intervertebral disc slice was subjected to a swelling phase where the disc equilibrated with its external saline environment for 33 hours followed by compression creep loading for an additional 33 hours. In general, fluid flowed into the disc during the free swelling stage of the theoretical experiment and was exuded
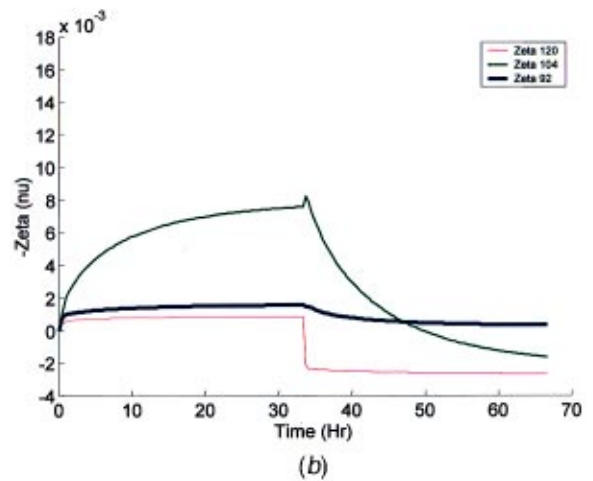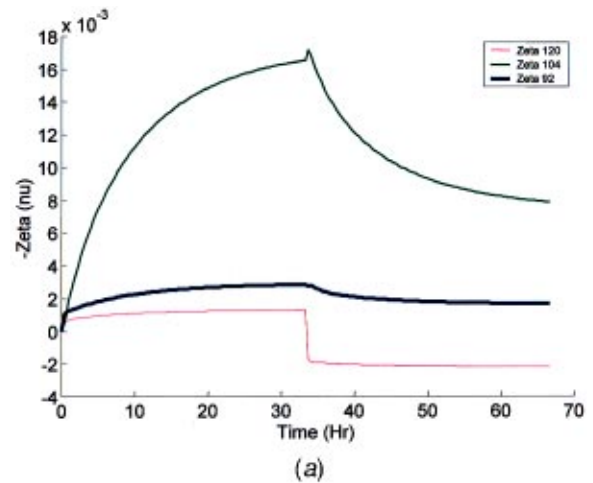

Fig. 4 Time history for the change in water content (-zeta) of the disc slice during the swelling phase and with creep loading for healthy (*a*) and degenerate (*b*) discs. The location of nodes 120, 104, and 92 are given in Fig. 2.

upon application of the constant compressive load (Fig. 4). The parameter zeta $\zeta = (dw_x/dx + dw_y/dy)$ is a measures of the net changes in water content of the tissue. It is important to note that, in this 2-D model, material behavior is strongly dependent on the nodal location and that is why curves in Fig. 4 appear differently. There was a net influx of fluid (i.e., negative value for zeta) for all nodes during the swelling phase of the experiments and a decrease in the absolute values for zeta during the compression stage. Isolating the transient fluid displacement behavior at node 104 (a node located toward the lateral inner portion of the disc see Fig. 2), we note there is a net influx of fluid (i.e., negative value for zeta) for the healthy disc and a net efflux (i.e., positive value for zeta) for the degenerate disc. At node 92 (antero-lateral outer location) there is less fluid transport and a small net influx of fluid at equilibrium (after both swelling and creep loading stages) for both healthy and degenerate fixed charge density distributions. Finally, for node 120 (posterolateral outer location), there is a net efflux out of the disc after equilibration of the compression loading.

The relative fluid displacement vectors were calculated for disc slices with healthy, degenerate, and equivalent healthy fixed charge density distributions (Fig. 5). For the healthy disc slice, it is clear that the net fluid displacement due to the osmotic pressure was inward even after the compressive load was applied. In the degenerate disc slice, however, the net fluid displacement was
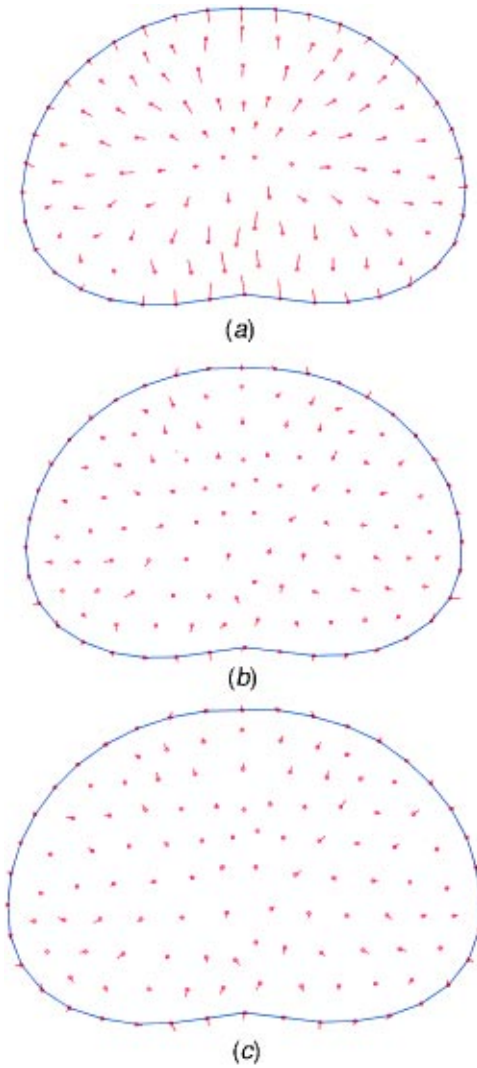
Fig. 5 Water displacement vectors for disc slices with (a) healthy fixed charge density (c^F), (b) degenerate c^F, and (c) constant equivalent healthy c^F. All plots are at the same scale with the maximum fluid displacement vector of w_{max}=0.005 m.
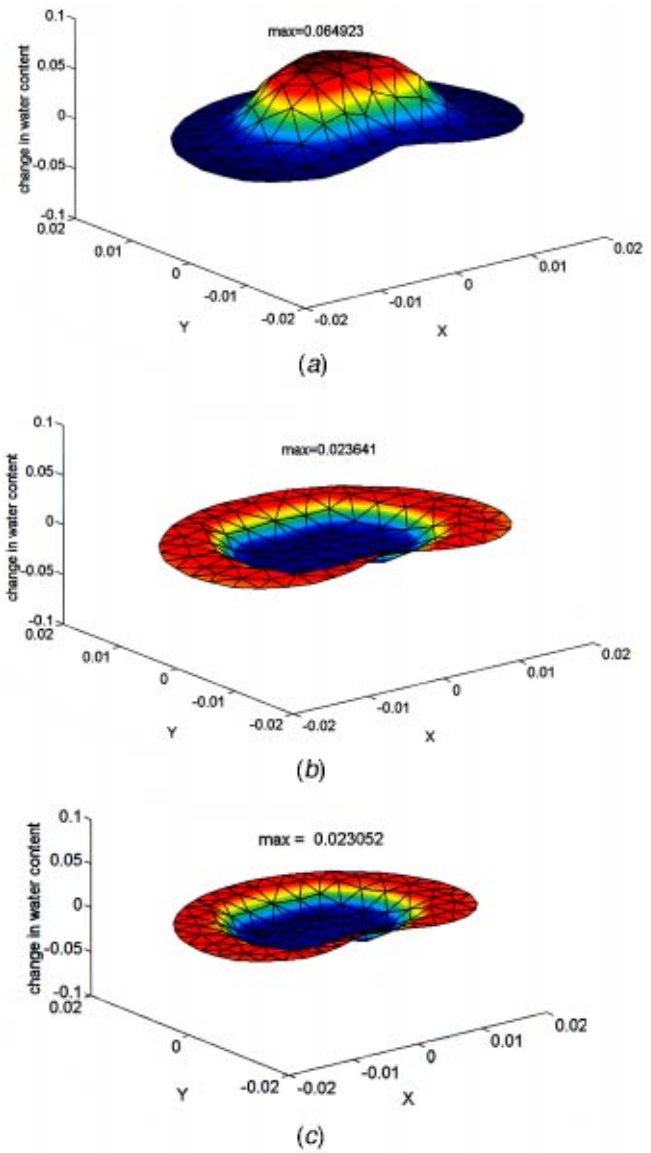

Fig. 6 Change in water content ($-\zeta$) for disc slices with (a) healthy, (b) degenerate, and (c) constant healthy equivalent fixed charge density distributions. Change in water content is measured after both swelling and compression stages of the experiment.

outward. Using the constant equivalent healthy fixed charge density distribution, fluid generally flowed outward and was similar in pattern to the degenerate case, suggesting that it is also the distribution of the fixed charges and not simply the magnitude that governs the fluid transport pattern in the disc. These fluid displacement vectors are useful for investigating the direction of fluid transport but for net changes in water content, the parameter zeta ζ is a more direct measurement (Fig. 6). Based on the results for ζ over the 2-D surface, it is apparent that the healthy fixed charge density results in a net increase in water content while both the degenerate and constant equivalent healthy fixed charge density results in a decrease in water content.

The equilibrium stress fields were also significantly affected by fixed charge density distribution (Fig. 7). The solid and fluid stresses sum to the total applied compressive stress (-200000 N/m^2). The healthy fixed charge density distribution generated a stress field with a very large gradient in solid stress and fluid pressure from the central nucleus pulposus to the outer annulus fibrosus (Figs. 7a, c). The large magnitude of fluid pressure in the nucleus and lower solid stress magnitude in the annulus indicates that most of the load is being carried by fluid pressurization, even at equilibrium. For the degenerate fixed charge density distribu-

tion, however, the gradient in solid stress and fluid pressurization was much smaller and the axial load was being carried predominantly by the solid matrix (Fig. 7b, d).

To determine the electrical potential field, the two sets of equations were alternately solved with fluid velocity passed to the $\Phi - c^n$ equations. During the transient period, the relative fluid velocity was not constant. When the relative fluid velocity was zero ($\dot{w}=0$), the steady state solution for Φ and c^n were simply constant at the prescribed boundary values. At a time just after the compressive load was applied, we have a nonzero $\dot{w}$. Using this $\dot{w}$ field in the $\Phi - c^n$ equations, we calculate a small but measurable potential field (Fig. 8). Current and ion concentration fields can also be calculated.

The applied electric potential results for the healthy and degenerate disc slices are shown in (Figs. 9, 10). These figures illustrates that fluid can be induced to flow through the disc by an altered potential on the boundary. In these tests, the applied po-
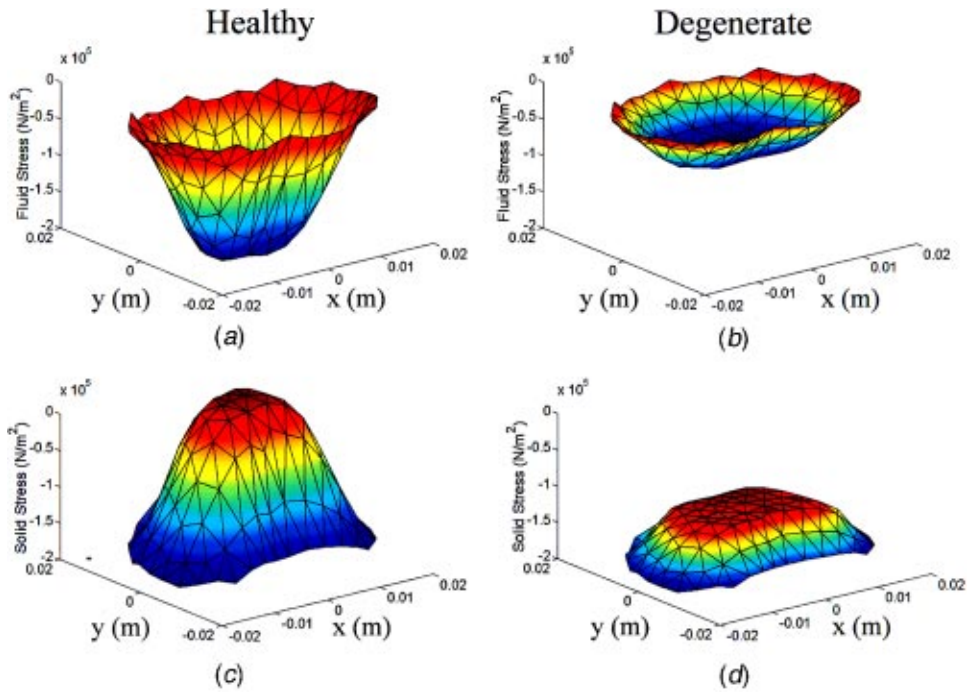
Fig. 7 Fluid (*a*, *b*) and solid (*c*, *d*) stress distributions for disc slices with healthy and degenerate fixed charge density distributions at equilibrium under compressive loading of −200,000 N/m². The fluid stress is equivalent to the negative of the pressure.

tential difference is extremely small, only about 10 mV and the maximum fluid velocity is only about 2.5×10^{-9} m/s. At this rate, the fluid would only move about 0.2 cm in a 24 hour period. For a 300 mV potential difference however, we expect forced convec-
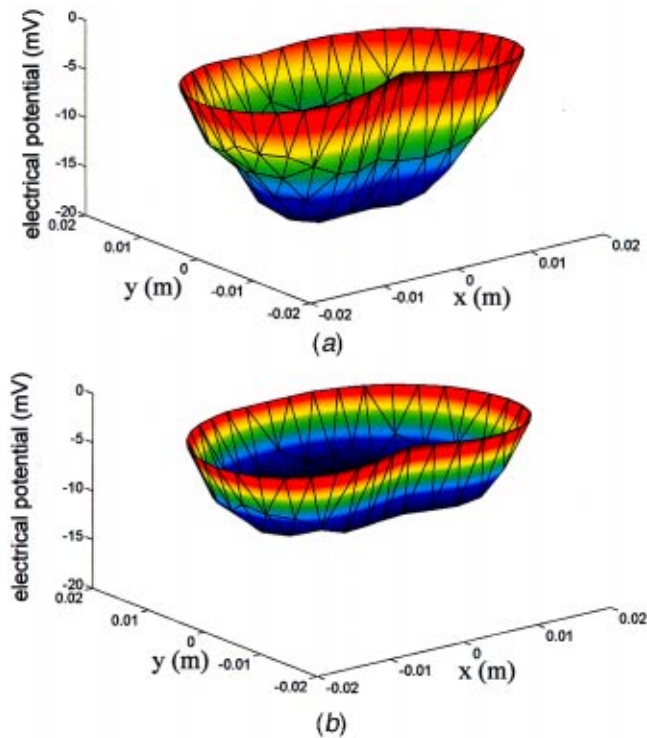
Fig. 8 Electric potential fields for (*a*) healthy and (*b*) degenerate disc slices subjected to swelling and compression loading immediately after the compressive load was applied.

Fig. 9 Electric potential field with applied potential difference across the right side of the disc slice with (*a*) healthy and (*b*) degenerate fixed charge density distribution. For the healthy disc the two potentials at A and B are 0 and −10.75 mV, respectively. For the degenerate disc the two potentials at A and B are 0 and −6.3 mV, respectively.

Fig. 10 Effect of applied electrical potential on water transport (dw/dt) for (*a*) healthy and (*b*) degenerated disc slices.
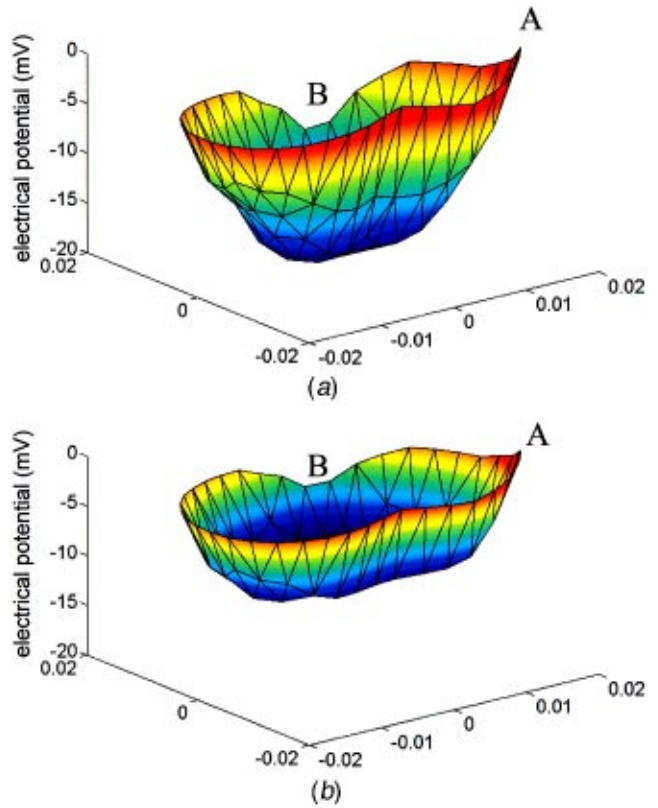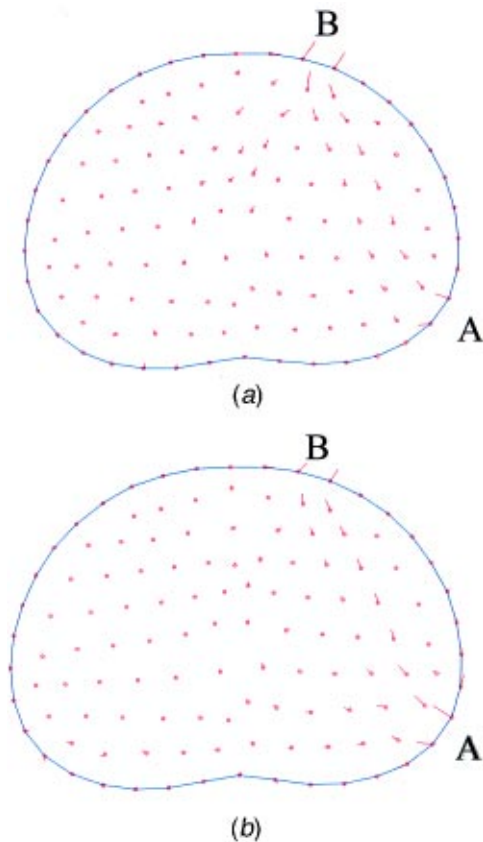
tion to transport fluid particles completely through a typical lumbar disc in a 24 hour period. It is important to note that while the fluid velocity fields are similar in healthy and degenerated discs (Fig. 10), the electrical potential fields (Fig. 9) are quite different.

4 Discussion

A 3-dimensional formulation for a poroelastic and chemical electric (PEACE) media was presented and applied to a intervertebral disc slice in a plane stress problem. The model was validated by comparing it with 1 dimensional experimental data. The model was then used to investigate the influence of fixed charge density magnitude and distribution on a slice of lumbar disc material. Results indicated that the mechanical, chemical, and electrical behaviors were strongly influenced by the amount as well as the distribution of fixed charges in the matrix. Without any other changes in material properties, alterations in the fixed charge density from a healthy to degenerate distribution will cause an increase in solid matrix stresses and can cause fluid loss from the tissue rather than imbibition. These differences as well as alterations in streaming potential have implications for disc nutrition, modulation of cellular activities, and tissue remodeling. It was also seen that application of an electrical potential across the disc can induce fluid transport. Application of this PEACE model underscores fact that even under simple loading conditions, 2- and 3-dimensional mechanical stress, strain, pressure, fluid velocity, electrical potential, and pH fields are present. These effects should be considered when investigating the influence of loading conditions on cellular metabolism.

Results of this study indicated that both the distribution and quantity of proteoglycans in the disc have a strong influence on fluid transport and load carriage mechanisms. Based on our studies, it is clear that both the magnitude and distribution of the fixed

charges are important factors in determining the direction of fluid flow (Fig. 6). Since transport of large solutes, such as hormones and enzymes, is affected by fluid flow within the disc [33], it is anticipated that a loss of fixed charge density will cause increased fluid efflux from the tissue and potentially a loss of important metabolites. The model also predicts that significantly more of the load is carried by hydrostatic pressure in the healthy disc relative to the disc with a degenerate fixed charge density distribution. This suggests that solid matrix stresses and strains will be larger in a disc with a degenerate fixed charge density distribution than in a disc with a healthy distribution.

Transport phenomena and other model behaviors will be strongly affected by the material property choice and boundary conditions. This study indicates that fluid transport is affected by fixed charge density and loading conditions. Electrical stimulation under zero applied load can also influence the fluid transport within the intervertebral disc. As shown (Fig. 10), even small applied electrical potential induces fluid transport in both normal and degenerated discs and could lead to an increased water content. These results may suggest potential minimally invasive treatment modalities where applied electrical potential induces forced convection that transports nutrients through degenerated discs. Indeed, while both healthy and degenerated discs have similar fluid velocity fields under the reported applied electrical potentials (Fig. 10), the electrical potential fields are different (Fig. 9), and cellular metabolism may be influenced by a host of other physical stimuli including pressures, electrical potential, solid matrix strains and stresses.

In the current model, there is only transport from the periphery of the disc which may explain the relatively long time constant for this 2-dimensional example described in this manuscript relative to experimental values for intervertebral discs in creep experiments [34]. Indeed, it has been reported that transport in the disc occurs more rapidly from the end-plate route than from the periphery [35]. The method of breaking down the system into smaller sets is sometimes called operator splitting and is sometimes used for solving large and complicated sets of equations. In this study we split the system such that the equations are broken into 2 smaller systems (2 equations in each) which are weakly coupled. We then solved the equations iteratively until convergence was achieved. The errors in the solution would be those primarily introduced by the finite element approximations and not the iterative solution technique. Coupling between these equations would be more significant under large displacements and significantly larger fluid velocities, but these limitations are not relevant in this paper. In this small strain, geometrically linear model, we do not account for strain dependent FCD, porosity, or permeability. The material properties used in this model are simplifications of the nonlinear, heterogeneous, and anisotropic behaviors found in the disc [6,11,36]

Degeneration of the disc will result in several material property changes to the annulus and nucleus [6,10,11,25,37,38] as well as alterations in fixed charge density [9]. A strength of the finite element model is the ability to parametrically alter one input factor and evaluate the effect on the results. Therefore, we have isolated the effect of fixed charge density amount and distribution alone. While this is not an entirely accurate representation of altered behaviors in the disc with highly progressed disc degeneration, it may provide an indication of early changes which could promote soft-tissue remodeling and a degenerative cascade. The values for fluid pressure, solid displacement and stresses, streaming potential, and sodium content presented in this study are similar to values reported in experimental studies [6,7,10,11,39,40]. This study shows the results of a 2-dimensional analysis, several additional complexities will be required to implement a more realistic 3-dimensional code including modification of the code to use three dimensional elements, as well as the use of anisotropic and nonlinear material properties. Some studies have utilized triphasic or multiphasic finite element models in one dimensional

configurations with model validation through experimental or other computational results (e.g., [20,30]). The PEACE model also demonstrated very good comparison with confined compression experimental behavior. The lack of model validation in 2-dimensions is a limitation and the magnitude of dependent variables should be interpreted with caution. The results of this study lay the framework for future experimental studies in two and three dimensions from which more complex and realistic disc behaviors can be studied and model validation also achieved. This study did effectively test our hypothesis that loss of intervertebral disc fixed charge density with degeneration leads to significant alterations in mechanical, chemical, and electrical behaviors of the disc through a parametric investigation using fixed charge density as the independent variable.

Nomenclature and Units

- a subscript implies per unit volume of mixture
- a superscript implies per unit volume of water
- s, w, p, n refer to the solid, water, positive ion and negative ion phases
- prefix: $m = 10^{-3}$
- prefix: $k = 10^{+3}$
- time: s (sec)
- length: m (meters)
- volume l (liters)
- mass: kg (kilograms)
- temperature: K (kelvin), body temperature. $= T = 273 + 37 = 310$ K
- force, Newton: $N = \mathrm{kg} - \mathrm{m}/s^2$
- densities: ρ_s, ρ_w, ρ_p, ρ_n (kg/m^3) are all per volume of the **mixture**.
- concentrations: c^F, c^p, c^n (moles/l) per volume of the solvent, c^p, $c^n = \mathrm{Na}^+$, Cl^- respectively
- fixed charge density: c^F: equivalent concentration of the negative fixed charges per volume of **solvent** (*moles/l*)
- electric field strength field strength: $E = \mathrm{mV}$
- electric potential: $\Phi = \mathrm{mN} - \mathrm{m}/\mathrm{coulomb}$
- Faraday's constant: $F = 96500$ coulombs/mole
- potentials: μ_w, μ_p, μ_n, μ_s (N $-$ m/kg) are scalar potential densities of the fluid, ion phases and the solid matrix
- drag coefficients: $f's$ are 3×3 diagonal matrices (N $- \mathrm{s}/\mathrm{m}^4$)
- inverse permeability:, $k_w =$ inverse permeability (N $-$ s/m^4)
- current flux: $I_e = 1$ coulomb/sec
- gas constant: $R = 8.31878 \times 10^3$ (m $-$ mN/mole $-$ K)

Appendix A: Mobility Equation and Coefficients

The terms in the mobility equation 11 and the relation to the friction coefficients is detailed below:

$$\begin{Bmatrix} \dot{w}_w \\ I_e \\ \dot{w}_p \\ \dot{w}_n \end{Bmatrix} = \begin{bmatrix} -\dfrac{1}{k_w} & F\nu_w & -\dfrac{k_p}{k_w} & -\dfrac{k_n}{k_w} \\ F\nu_w & F^2(\nu_p c^p - \nu_n c^n) & F\nu_p & F\nu_n \\ -\dfrac{k_p}{k_w} & F\nu_p & -\dfrac{\alpha_p}{D/n} & -\dfrac{f_{w,n}f_{w,p}}{D/n} \\ -\dfrac{k_n}{k_w} & F\nu_n & -\dfrac{f_{w,n}f_{w,p}}{D/n} & -\dfrac{\alpha_n}{D/n} \end{bmatrix}$$

$$\times \begin{Bmatrix} \rho_w \nabla \mu_w \\ n\nabla \Phi \\ nRT\nabla c^p \\ nRT\nabla c^n \end{Bmatrix}$$

where:

$$k_n = \frac{f_{w,n}}{f_{n,s} + f_{w,n}}, \quad k_p = \frac{f_{w,p}}{f_{p,s} + f_{w,p}}$$

$$k_w = \frac{1}{n}\left(f_{s,w} + \frac{f_{p,s}f_{w,p}}{f_{p,s} + f_{w,p}} + \frac{f_{n,s}f_{w,n}}{f_{n,s} + f_{w,n}} \right)$$

$$\nu_w = \frac{c^n f_{w,n}(f_{p,s} + f_{w,p}) - c^p f_{w,p}(f_{n,s} + f_{w,n})}{D/n} = -\left(\frac{k_p}{k_w} c^p - \frac{k_n}{k_w} c^n \right)$$

$$\nu_p = \frac{c^n f_{w,n}f_{w,p} - c^p \alpha_p}{D/n} \qquad \nu_n = \frac{c^n \alpha_n - c^p f_{w,p}f_{w,n}}{D/n}$$

$$\alpha_p = (f_{n,s} + f_{w,n})f_{s,w} + f_{w,p}f_{n,s} + (f_{w,p} + f_{n,s})f_{w,n}$$

$$\alpha_n = (f_{p,s} + f_{w,p})f_{s,w} + f_{w,p}f_{p,s} + (f_{p,s} + f_{w,p})f_{w,n}$$

$$D = f_{s,w}f_{p,s}f_{n,s} + f_{s,w}f_{p,s}f_{w,n} + f_{s,w}f_{w,p}f_{n,s} + f_{s,w}f_{w,p}f_{w,n}$$
$$+ f_{w,p}f_{p,s}f_{n,s} + f_{w,p}f_{p,s}f_{w,n} + f_{w,n}f_{p,s}f_{n,s} + f_{w,n}f_{w,p}f_{n,s}$$

$$k_w = \frac{\alpha}{(1 + b_w)}, \quad k_p = \frac{b_p}{(1 + b_w)}, \quad k_n = \frac{b_n}{(1 + b_w)},$$

$$\alpha = \frac{(f_{s,w} + f_{w,p} + f_{w,n})}{n}$$

$$b_w = \frac{f_{w,p}^2 f_{n,s} + f_{w,p}^2 f_{w,n} + f_{w,n}^2 f_{p,s} + f_{w,n}^2 f_{w,p}}{D},$$

$$b_p = \frac{f_{w,p}(\alpha_p + f_{w,n}^2)}{D}, \quad b_n = \frac{f_{w,n}(f_{w,p}^2 + \alpha_n)}{D}$$

Appendix B: PEACE Field Equations. The four field equations (12–15) in a matrix form are:

$$
\begin{bmatrix}
0 & 0 & 0 & 0 \\
0 & -K_{w,w} & 0 & 0 \\
0 & -\nabla \cdot K_{\phi,w} & 0 & 0 \\
0^* & +\nabla \cdot K_{n,w} & 0 & n
\end{bmatrix}
\begin{pmatrix} \dot{\mathbf{u}} \\ \dot{\mathbf{w}} \\ \dot{\boldsymbol{\Phi}} \\ \dot{c}^n \end{pmatrix}
+
\begin{bmatrix}
L^T D_{\varepsilon,\varepsilon} L & L^T D_{\varepsilon,\zeta} \nabla \cdot & 0 & 0 \\
\nabla D_{\zeta,\varepsilon} L & \nabla D_{\zeta,\zeta} \nabla \cdot & -K_{w,\phi} \nabla & -(K_{w,p}+K_{w,n}) \nabla \\
0 & 0 & -\nabla \cdot K_{\phi,\phi} \nabla & -\nabla \cdot (K_{\phi,p}+K_{\phi,n}) \nabla \\
0 & 0 & -\nabla \cdot K_{n,\phi} \nabla & -\nabla \cdot (K_{n,p}+K_{n,n}) \nabla
\end{bmatrix}
\begin{pmatrix} \mathbf{u} \\ \mathbf{w} \\ \Phi \\ c^n \end{pmatrix}
+
\begin{pmatrix} 0 \\ -K_{w,p} \nabla \\ -\nabla \cdot K_{\phi,p} \nabla \\ -\nabla \cdot K_{n,p} \nabla \end{pmatrix} c^F
$$

$$
+
\begin{pmatrix} L^T \boldsymbol{\sigma}_{o\sigma} \\ \nabla \sigma_{o\pi} \\ 0 \\ 0 \end{pmatrix}
=
\begin{pmatrix} 0 \\ 0 \\ 0 \\ 0 \end{pmatrix}
\tag{21}
$$

where:

$$
K_{w,w} = \widetilde{k}_w = \frac{k_w}{n} \qquad K_{n,w} = c^n k_n \qquad K_{\phi,w} = \nu_w k_w F
$$

$$
K_{w,\phi} = F(k_p c^p - k_n c^n) \qquad K_{n,\phi} = c^n k_{n,\phi} nF \qquad K_{\phi,\phi} = n k_{\phi,\phi} F^2
$$

$$
K_{w,p} = k_p RT \qquad K_{n,p} = c^n k_{n,p} nRT \qquad K_{\phi,p} = n k_{\phi,p} FRT
$$

$$
K_{w,n} = k_n RT \qquad K_{n,n} = c^n k_{n,n} nRT \qquad K_{\phi,n} = n k_{\phi,n} FRT
$$

$$
k_{\phi,p} = \nu_w k_p - \nu_p \qquad k_{\phi,n} = \nu_w k_n - \nu_n \qquad k_{\phi,\phi} = k_{\phi,p} c^p - k_{\phi,n} c^n
$$

$$
k_{n,\phi} = -\frac{k_n k_p c^p - k_n^2 c^n + \nu_n k_w}{k_w} \qquad k_{n,n} = \frac{\alpha_n n k_w - k_n^2 D}{k_w D} \qquad k_{p,n} = \frac{f_{w,n} f_{w,p}}{D/n} - \frac{k_p k_n}{k_w} = k_{n,p}
$$

$$
\sigma_{o\pi} = \pi^2, \quad \boldsymbol{\sigma}_{o\sigma} = \{0\}_{6x1} \qquad 0^* = c^n \nabla \cdot \qquad \dot{e} = \nabla \cdot \dot{\mathbf{u}}
$$

$$
\rho_w \nabla \mu_w = -n \nabla \pi, \quad \dot{w}_w = n(v_w - v_s), \quad \dot{w}_p = n(v_p - v_s), \quad \dot{w}_n = n(v_n - v_s)
$$

$$
I_e = F(c^p \dot{w}_p - \dot{w}_n c^n), \quad E = -\nabla \Phi, \quad \rho_p \nabla \mu_p = nRT \nabla c^p, \quad \rho_n \nabla \mu_n = nRT \nabla c^n,
$$

$$
\pi = \pi^f + \pi^c, \quad \pi^f = -p, \quad \pi^c = -\rho_{w\mathbf{T}} \mu_{w,0} + RT\phi(2c^n + c^F) + B_w \zeta + T_c
$$

$$
\pi^f = \alpha Q \mathbf{m}^T \mathbf{e} + Q\zeta, \quad T_c = a_0 c^F \exp[-\kappa(\gamma_{\pm}/\gamma_{\pm}^*)\sqrt{c^n(c^n + c^F)}] - P_{\infty}
$$

$$
\begin{Bmatrix} \sigma_{x,x} \\ \sigma_{y,y} \\ \sigma_{z,z} \\ \sigma_{x,y} \\ \sigma_{y,z} \\ \sigma_{z,x} \\ \pi \end{Bmatrix}
=
\begin{bmatrix}
\lambda+2\mu+Q & \lambda+Q & \lambda+Q & 0 & 0 & 0 & Q \\
\lambda+Q & \lambda+2\mu+Q & \lambda+Q & 0 & 0 & 0 & Q \\
\lambda+Q & \lambda+Q & \lambda+2\mu+Q & 0 & 0 & 0 & Q \\
0 & 0 & 0 & \mu & 0 & 0 & 0 \\
0 & 0 & 0 & 0 & \mu & 0 & 0 \\
0 & 0 & 0 & 0 & 0 & \mu & 0 \\
Q & Q & Q & 0 & 0 & 0 & Q
\end{bmatrix}
\begin{Bmatrix} \varepsilon_{x,x} \\ \varepsilon_{y,y} \\ \varepsilon_{z,z} \\ \varepsilon_{x,y} \\ \varepsilon_{y,z} \\ \varepsilon_{z,x} \\ \zeta \end{Bmatrix}
+
\begin{Bmatrix} 0 \\ 0 \\ 0 \\ 0 \\ 0 \\ 0 \\ \pi^c \end{Bmatrix}
$$

$$
D_{\varepsilon,\varepsilon} =
\begin{bmatrix}
\lambda+2\mu+Q & \lambda+Q & \lambda+Q & 0 & 0 & 0 \\
\lambda+Q & \lambda+2\mu+Q & \lambda+Q & 0 & 0 & 0 \\
\lambda+Q & \lambda+Q & \lambda+2\mu+Q & 0 & 0 & 0 \\
0 & 0 & 0 & \mu & 0 & 0 \\
0 & 0 & 0 & 0 & \mu & 0 \\
0 & 0 & 0 & 0 & 0 & \mu
\end{bmatrix}
\qquad
\begin{array}{l}
D_{\zeta,\varepsilon} = Q\mathbf{m}^T \\
D_{\varepsilon,\zeta} = D_{\zeta,\varepsilon}^T \\
D_{\zeta,\zeta} = Q \\
\nabla = grad = (\nabla \cdot)^T
\end{array}
$$

$$
L^T =
\begin{bmatrix}
\dfrac{\partial}{\partial x} & 0 & 0 & \dfrac{\partial}{\partial y} & 0 & \dfrac{\partial}{\partial z} \\
0 & \dfrac{\partial}{\partial y} & 0 & \dfrac{\partial}{\partial x} & \dfrac{\partial}{\partial z} & 0 \\
0 & 0 & \dfrac{\partial}{\partial z} & 0 & \dfrac{\partial}{\partial y} & \dfrac{\partial}{\partial x}
\end{bmatrix},
\qquad
\begin{array}{c}
\nabla \cdot = div = \left| \dfrac{\partial}{\partial x} \quad \dfrac{\partial}{\partial y} \quad \dfrac{\partial}{\partial z} \right| \\[2mm]
\sigma^s = [\sigma_{xx} \ \sigma_{yy} \ \sigma_{zz} \ \sigma_{xy} \ \sigma_{yz} \ \sigma_{zx}]^T \\[2mm]
\mathbf{e} = [\varepsilon_{xx} \ \varepsilon_{yy} \ \varepsilon_{zz} \ \varepsilon_{xy} \ \varepsilon_{yz} \ \varepsilon_{zx}]^T
\end{array}
$$

$$\lambda = \frac{\nu E}{(1+\nu)(1-2\nu)}, \quad \mu = \frac{E}{2(1+\nu)} \qquad \mathbf{m} = [1 \quad 1 \quad 1 \quad 0 \quad 0 \quad 0]^T$$

$$\zeta = \nabla \cdot \mathbf{w}, \quad \mathbf{e} = L\mathbf{u}, \quad \mathbf{u} = [u_x u_y u_z]^T, \quad \mathbf{w} = [w_x w_y w_z]^T, \quad e = m^T \mathbf{e}$$

Appendix C: PEACE Field Equations, Finite Element Form

Application of the Galerkin FEM procedure to the field equations 21, with integration by parts to second order terms yield the following nonlinear matrix equation:

$$\int \begin{bmatrix} 0 & 0 & 0 & 0 \\ 0 & N^T K_{w,w} N & 0 & 0 \\ 0 & (\nabla N)^T K_{\phi,w} N d\Omega & 0 & 0 \\ (N^T c^n \nabla N)^* & N^T (\nabla \cdot K_{n,w}) N & 0 & N^T n N \end{bmatrix} d\Omega \begin{pmatrix} \mathbf{u} \\ \mathbf{w} \\ \Phi \\ \mathbf{c}^n \end{pmatrix}$$

$$+ \int \begin{bmatrix} (LN)^T D_{\varepsilon,\varepsilon}(LN) & (LN)^T D_{\varepsilon,\zeta} \nabla N & 0 & 0 \\ (\nabla N)^T D_{\varepsilon,\varepsilon}(LN) & (\nabla N)^T D_{\zeta,\zeta} \nabla N & N^T K_{w,\phi} \nabla N & N^T (K_{w,n} + K_{w,p}) \nabla N \\ 0 & 0 & (\nabla N)^T K_{\phi,\phi} \nabla N & (\nabla N)^T (K_{\phi,n} + K_{\phi,p}) \nabla N \\ 0 & 0 & (\nabla N)^T K_{n,\phi} \nabla N & (\nabla N)^T (K_{n,n} + K_{n,p}) \nabla N \end{bmatrix} d\Omega \begin{pmatrix} \mathbf{u} \\ \mathbf{w} \\ \Phi \\ \mathbf{c}^n \end{pmatrix}$$

$$= \begin{pmatrix} -\int (LN)^T \sigma_{o\sigma} d\Omega \\ -\int (\nabla N)^T \sigma_{o\pi} d\Omega \\ 0 \\ 0 \end{pmatrix} + \begin{pmatrix} 0 \\ -\int N^T K_{w,p} \nabla N d\Omega c^F \\ -\int (\nabla N)^T K_{\phi,p} \nabla N d\Omega c^F \\ \int (\nabla,N)^T K_{n,p} \nabla N d\Omega c^F \end{pmatrix} + \begin{pmatrix} +\int N^T T_\sigma d\Gamma \\ +\int N^T T_\pi d\Gamma \\ -\int N^T I_e d\Gamma \\ +\int N^T q_{ndiff} d\Gamma \end{pmatrix} \qquad (22)$$

$$\sigma_{o\pi} = \pi^c = -\rho_{w\mathbf{T}} \mu_{w,0} + RT\phi(2c^n + c^F) + B_w \zeta + T_c$$

$$T_c = a_0 c^F \exp[-\kappa(\gamma_\pm / \gamma_\pm^*) \sqrt{c^n(c^n + c^F)}] - P_\infty$$

$$\sigma_{o\sigma} = 0$$

$T_\sigma =$ applied compressive load, eg. -200000N/m^2

$T_\pi =$ applied mechanical fluid/chemical pressure (includes bath osmotic pressure)

$I_e =$ imposed current, eg. 0 (Φ is imposed by Potential Equilibrium)

$q_{ndiff} =$ applied flux of c_n, eg. 0 (c_n is imposed by Donnan Equilibrium)

A subtle point is necessary. In the first matrix of equation 22, the term $(N^T c^n \nabla N)^*$ in position 4, 1 should be 0 when the term in position 4, 2 is $N^T(\nabla \cdot K_{n,w})N$ as shown. When the term in position 4, 1 is $N^T c^n \nabla N$, then the term in position 4, 2 should read $N^T(\nabla \cdot K_{n,w})N + N^T K_{n,w} \nabla N$.

References

[1] Frymoyer, J. W., and Cats-Baril, W. L., 1991, "An Overview of Incidences and Costs of Low Back Care," Orthop. Clin. North Am., **22**, pp. 263–271.
[2] Rutlow, I. M., 1986, "Orthopaedic Operations in the United States 1979–1983," J. Bone Jt. Surg., **68A**, pp. 716–719.
[3] Antoniou, J., Steffen, T., Nelson, F., Winterbottom, N., Hollander, A., Poole, R. A., Aebi, M., and Alini, M., 1996, "The Human Lumbar Disc: Evidence for Changes in the Biosynthesis and Denaturation of the Extracellular Matrix with Growth, Maturation, Ageing, and Degeneration," J. Clin. Invest., **98**, pp. 996–1003.
[4] Lyons, G., Eisenstein, S., and Sweet, M., 1981, "Biochemical Changes in Intervertebral Disc Degeneration," Biochim. Biophys. Acta, **673**, pp. 443–453.
[5] Urban, J. P. G., and Holm, S. H., 1986, "Intervertebral Disc Nutrition as Related to Spinal Movements and Fusion," Tissue Nutrition and Viability, Edited by AR Hargens, New York, NY, Springer-Verlag, pp. 101–119.
[6] Iatridis, J. C., Setton, L. A., Foster, R. J., Rawlins, B. A., Weidenbaum, M., and Mow, V. C., 1998, "Degeneration Affects the Anisotropic and Nonlinear Behaviors of Human Anulus Fibrosus in Compression," J. Biomech., **31**, pp. 535–544.
[7] Nachemson, A., 1960, "Lumbar Intradiscal Pressure," Acta Orthop. Scand. Suppl., **43**, pp. 1–104.
[8] Panjabi, M., Brown, M., Lindahl, S., Irstam, L., and Hermens, M., 1988, "Intrinsic Disc Pressure as a Measure of Integrity of the Lumbar Spine," Spine, **13**, pp. 913–917.
[9] Urban, J. P. G., and McMullin, J. F., 1988, "Swelling Pressure of the Lumbar Intervertebral Discs: Influence of Age, Spinal Level, Composition, and Degeneration," Spine, **13**, 179–187.
[10] Gu, W. Y., Mao, X. G., Rawlins, B. A., Iatridis, J. C., Foster, R. J., Sun, D. N., Weidenbaum, M., and Mow, V. C., 1999, "Streaming Potential of Human Lumbar Anulus Fibrosus is Anisotropic and Affected by Disc Degeneration," J. Biomech., **32**, pp. 1177–1182.
[11] Gu, W. Y., Mao, X. G., Foster, R. J., Weidenbaum, M., Mow, V. C., and Rawlins, B. A., 1999, "The Anisotropic Hydraulic Permeability of Human Lumbar Anulus Fibrosus. Influence of Age, Degeneration, Direction, and Water Content," Spine, **24**, pp. 2449–2455.
[12] Frank, E. H., and Grodzinsky, A. J., 1987, "Cartilage Electromechanics. I. Electrokinetic Transduction and the Effect of Electrolyte pH and Ionic Strength," J. Biomech., **20**, pp. 615–627.
[13] Frank, E. H., and Grodzinsky, A. J., 1987, "Cartilage Electromechanics. II. A Continuum Model of Cartilage Electrokinetics and Correlation with Experiments," J. Biomech., **20**, pp. 629–639.
[14] Gu, W. Y., Lai, W. M., and Mow, V. C., 1993, "Transport of Fluid and Ions Through a Porous-permeable Charged-hydrated Tissue and Streaming Potential Data on Normal Bovine Articular Cartilage," J. Biomech., **26**, pp. 709–723.
[15] Lai, W. M., Hou, J. S., and Mow, V. C., 1991, "A Triphasic Theory for the Swelling and Deformation Behavior of Articular Cartilage," ASME J. Biomech. Eng., **113**, pp. 245–258.

[16] Maroudas, A., 1979, ''Physicochemical Properties of Articular Cartilage,'' Adult Articular Cartilage, Edited by Freeman MAR, Kent, U.K., Pitman Medical, pp. 215–290.

[17] Urban, J. P. G., Maroudas, A., Bayliss, M. T., and Dillon, J., 1979, ''Swelling Pressures of Proteoglycans at the Concentrations Found in Cartilaginous Tissues,'' Biorheology, **16**, pp. 447–464.

[18] Argoubi, M., and Shirazi-Adl, A., 1996, ''Poroelastic Creep Response Analysis of a Lumbar Motion Segment in Compression,'' J. Biomech., **29**, pp. 1331–1339.

[19] Best, B. A., Guilak, F., Setton, L. A., Zhu, W., Saed-Nejad, F., Radcliffe, A., Weidenbaum, M., and Mow, V. C., 1994, ''Compressive Mechanical Properties of the Human Annulus Fibrosus and Their Relationship to Biochemical Composition,'' Spine, **19**, pp. 212–221.

[20] Frijns, A. J. H., Huyghe, J. M., and Janssen, J. D., 1997, ''A Validation of the Quadriphasic Mixture Theory for Intervertebral Disc Tissue,'' Int. J. Eng. Sci., **35**, pp. 1419–1429.

[21] Laible, J. P., Pflaster, D., Krag, M. H., Simon, B. R., and Haugh, L. D., 1993, ''A Poroelastic-swelling Finite Element Model with Application to the Intervertebral Disc,'' Spine, **18**, pp. 659–670.

[22] Laible, J. P., Pflaster, D., Simon, B. R., Krag, M. H., Pope, M. H., and Haugh, L. D., 1994, ''A Dynamic Material Parameter Estimation Procedure for Soft Tissue Using a Poroelastic Finite Element Model,'' ASME J. Biomech. Eng., **116**, pp. 19–29.

[23] Simon, B. R., Wu, J. S., Carlton, M. W., Evans, J. H., and Kazarian, L. E., 1985, ''Structural Models for Human Spinal Motion Segments Based on a Poroelastic View of the Intervertebral Disc,'' ASME J. Biomech. Eng., **107**, pp. 327–335.

[24] Snijders, H., Huyghe, J. M., and Janssen, J. D., 1995, ''Triphasic Finite Element Model for Swelling of Porous Media,'' Int. J. Numer. Methods Fluids, **20**, pp. 1039–1046.

[25] Iatridis, J. C., Setton, L. A., Weidenbaum, M., and Mow, V. C., 1997, ''Alterations in the Mechanical Behavior of the Human Lumbar Nucleus Pulposus with Degeneration and Aging,'' J. Orthop. Res., **15**, pp. 318–322.

[26] Biot, M. A., 1962, ''Mechanics of Deformation and Acoustic Propagation in Porous Media,'' J. Appl. Phys., **33**, pp. 1482–1498.

[27] Biot, M. A., 1972, ''Theory of Finite Deformation of Porous Soils,'' Indiana Univ. Math. J., **21**, pp. 597–620.

[28] Simon, B. R., 1992, ''Multi-phase Poroelastic Finite Element Models for Soft Tissue Structures,'' Appl. Mech. Rev., **45**, pp. 191–219.

[29] Simon, B. R., Laible, J. P., Pflaster, D., Yuan, Y., and Krag, M., 1996, ''A Poroelastic Finite Element Formulation Including Transport Swelling in Soft Tissue Structures,'' ASME J. Biomech. Eng., **118**, pp. 1–9.

[30] Sun, D. N., Gu, W. Y., Guo, X. E., Lai, W. M., and Mow, V. C., 1999, ''A Mixed Finite Element Formulation of Triphasic Mechano-electrochemical Theory for Charged, Hydrated Biological Soft Tissues,'' Int. J. Numer. Methods Eng., **45**, pp. 1375–1402.

[31] Huyghe, J. M., and Janssen, J. D., 1997, ''Quadriphasic Mechanics of Swelling Incompressible Porous Media,'' Int. J. Eng. Sci., **35**, pp. 793–802.

[32] Drost, M. R., Willems, P., Snijders, H., Huyghe, J. M., Janssen, J. D., and Huson, A., 1995, ''Confined Compression of Canine Annulus Fibrosus Under Chemical and Mechanical Loads,'' ASME J. Biomech. Eng., **117**, pp. 390–396.

[33] Urban, J. P. G., Holm, S., Maroudas, A., and Nachemson, A., 1982, ''Nutrition of the Intervertebral Disc: Effect of Fluid Flow on Solute Transport,'' Clin. Orthop. Relat. Res., **170**, pp. 296–302.

[34] Keller, T., Spengler, D., and Hansson, T., 1987, ''Mechanical Behavior of the Human Lumbar Spine. I. Creep Analysis During Static Compressive Loading,'' J. Orthop. Res., **5**, pp. 467–478.

[35] Holm, S., Maroudas, A., Urban, J. P. G., Selstam, G., and Nachemson, A., 1981, ''Nutrition of the Intervertebral Disc: Solute Transport and Metabolism,'' Connect. Tissue Res., **8**, pp. 101–119.

[36] Elliott, D. M., and Setton, L. A., 2001, ''Anisotropic and Inhomogeneous Tensile Behavior of the Human Anulus Fibrosus: Experimental Measurement and Material Model Predictions,'' ASME J. Biomech. Eng., **23**, pp. 256–263.

[37] Acaroglu, E., Iatridis, J. C., Setton, L. A., Foster, R., Mow, V. C., and Weidenbaum, M., 1995, ''Degeneration and Aging Affect the Tensile Behavior of Human Lumbar Annulus Fibrosus,'' Spine, **20**, pp. 2690–2701.

[38] Galante, J., 1967, ''Tensile Properties of the Human Lumbar Anulus Fibrosus,'' Acta Orthop. Scand., **100**, pp. 68–82.

[39] Kraemer, J., Kolditz, D., and Gowin, R., 1985, ''Water and Electrolyte Content of Human Intervertebral Discs Under Variable Load,'' Spine, **10**, pp. 69–71.

[40] Krag, M., Seroussi, R., Wilder, D., and Pope, M., 1987, ''Internal Displacement Distribution from in Vitro Loading of Human Thoracic and Lumbar Spinal Motion Segments: Experimental Results and Theoretical Predictions,'' Spine, **12**, pp. 1001–1007.